NJC

Prussian blue as a co-catalyst for enhanced Cr (VI) photocatalytic reduction promoted by titania-based nanoparticles and aerogels

Journal:	*New Journal of Chemistry*
Manuscript ID	NJ-ART-03-2021-001141.R1
Article Type:	Paper
Date Submitted by the Author:	22-Apr-2021
Complete List of Authors:	Ferreira Neto, Elias; Institute of Chemistry of São Carlos, Molecular Physics and Chemistry Ullah, Sajjad; University of Peshawar, Chemical Sciences; Universidade Paulista, General and Inorganic Chemistry Perissinotto, Amanda; University of Sao Paulo, Institute of Chemistry of São Carlos de Vicente, Fabio; Sao Paulo State University Julio de Mesquita Filho, Institute of Geosciences and Exact Sciences, Department of Physics Ribeiro, Sidney; Universidade Estadual Paulista Julio de Mesquita Filho Instituto de Quimica, Worsley, Marcus; Lawrence Livermore National Laboratory, Physical and Life Sciences Directorate Rodrigues-Filho, Ubirajara; Universidade de Sao Paulo Instituto de Quimica de Sao Carlos, 2 Grupo de Química de Materiais Híbridos e Inorgânicos

Prussian blue as a co-catalyst for enhanced Cr (VI) photocatalytic reduction promoted by titania-based nanoparticles and aerogels

Elias Paiva Ferreira-Neto[a,b*], Sajjad Ullah[b,c,d] Amanda Pasquoto Perissinotto[a], Fábio S. de Vicente[e], Sidney José Lima Ribeiro[b], Marcus Andre Worsley[f], Ubirajara Pereira Rodrigues-Filho[a*]

[a]Institute of Chemistry of São Carlos, University of São Paulo, 13560-970, São Carlos, SP, Brazil

[b]Institute of Chemistry, São Paulo State University (UNESP), 14800-060, Araraquara, SP, Brazil

[c]Institute of Chemical Sciences, University of Peshawar, PO Box 25120, Peshawar, Pakistan

[d]Institute of Physics, Federal University of Mato Grosso do Sul, 79070-900, Campo Grande, MS, Brazil

[e]Institute of Geosciences and Exact Sciences, Department of Physics, São Paulo State University (UNESP), 13506-970, Rio Claro, SP, Brazil

[f]Physical and Life Sciences Directorate, Lawrence Livermore National Laboratory, 94550, Livermore, CA, USA

*Corresponding authors: elias.p.ferreira@gmail.com (E. P. Ferreira-Neto), ubirajara@usp.br (U. P. Rodrigues-Filho)

Abstract

Hexavalent Chromium (Cr(VI)) is an obnoxious and highly toxic heavy metal that presents a serious threat to human health if present even in low concentrations in drinking water. Photocatalytic reduction of Cr(VI) to its less toxic Cr(III) state is a potential strategy to combat Cr(IV) pollution, but the efficiency of the process in low, especially in the absence of hole scavenger organic reagents. To address this issue and prepare efficient photocatalysts for Cr(VI) removal from water, in this study, we explored Prussian blue (PB) as a co-catalyst for improving the photoreduction performance of different high surface area TiO_2-based materials (titania or silica-titania nanoparticles and aerogels). The photocatalysts nanomaterials were surface-modified with nanocrystalline PB using photodeposition route. PB layer acts as an effective electron acceptor/mediator between semiconductor photocatalyst and Cr(VI) species. All the PB-modified photocatalysts exhibit higher photocatalytic activity (up to 9 times faster) as compared to unmodified photocatalysts towards reduction of Cr (VI). Importantly, the PB-modified photocatalysts exhibited high photocatalytic performance (98-99% reduction in 40min for pH = 5.6 and in 10 min for pH=3) without addition of organic reagents. The simple approach reported herein can be followed to prepare new PB-photocatalyst systems with improved photocatalytic performance towards Cr (VI) reduction and other target applications.

1. Introduction

Pollution of fresh water bodies by a variety of toxic organic (dyes, pharmaceutical products, pesticides) and inorganic (heavy metals) contaminants is a serious environmental challenge of great concern that requires immediate attention. Water pollutants has not only affected aquatic life, consumption of contaminated water bodies has also been associated with numerous health ailments in humans [1–3]. Among the heavy metals, hexavalent chromium (Cr(VI)) is a highly toxic and carcinogenic contaminant commonly present in wastewater from different industrial activities such as electroplating, pigment production, leather tanning, mining, metallurgy and others [4,5]. Owing to their high solubility and high mobility in water, Cr(VI) species are difficult to be removed from water bodies and present a serious threat to human health if present even in low concentrations in drinking water. On the other hand, Cr(III) species exhibit lower toxicity and can be easily removed by precipitation as $Cr(OH)_3$ employing conventional water treatment techniques. Thus, treatment of Cr(VI) contaminants essentially involves reduction of Cr(VI) to Cr(III) species using different reductive removal methodologies such as bioremediation, electrocatalysis, chemical precipitation and photocatalysis [6].

Heterogeneous photocatalysis is regarded as a promising and sustainable approach for environmental remediation as it is (ideally) capable of promoting water purification by harnessing solar energy and employing only water and oxygen as reagents [7]. Upon photoexcitation with light of suitable energy, an electron is promoted from the valence band (VB) to the conduction band (CB) of the photocatalysts, thus generating oxidative holes (in VB) and reductive electrons (in CB) which are capable of promoting the oxidative breakdown of organic pollutants and photocatalytic reduction reactions, respectively[8]. The photocatalytic reduction ability of photocatalysts can be usefully exploited for removal of heavy metals contaminants from water bodies [9]. In particular, several studies have reported the photocatalytic reduction of Cr(VI) using semiconductor catalysts as a promising approach for the treatment of chromate contaminated wastewater. Despite the great potential of photocatalysis for the removal of heavy metal pollutants, particularly Cr(VI) from water, the overall efficiency of such photocatalytic processes is still low and it is often necessary to add organic additives (as electron donors) and perform the reduction process in acidic media to achieve the desirable efficiency [6,10–12]. Doing so, however, offsets the advantages offered by the photocatalytic process and raises concern over the feasibility of photocatalytic wastewater treatment. Thus, it is of great interest to develop new, cost-effective and more efficient photocatalytic systems that could be employed in wastewater treatment without requiring the addition of organic additives or acids during the photocatalytic reduction processes or other environmental applications.[13]

Among the heterogeneous photocatalysts employed for environmental remediation applications, TiO_2–based nanomaterials are still the most widely studied photocatalysts due to their relatively higher photocatalytic efficiency and other desirable characteristics including good (photo)chemical stability, low-cost and ease of preparation, among others [14,15]. Nevertheless, a number of drawbacks associated with the use of TiO_2 limit its performance as a photocatalyst. These limitations of TiO_2 may be related to its physical properties (nanoparticle agglomeration, uncontrolled crystallite growth and phase transformation during thermal treatments) [16–18] or its intrinsic electronic properties (lack of visible light photoactivity, high rate of electron-hole recombination) [19,20]). Both of these characteristics of TiO_2 diminish the quantum yield of the photocatalytic

process and lower the probability of multi-electron redox reactions (including Cr(VI) reduction) to occur. Formation of nanocomposite materials by modification of TiO_2 with metal nanoparticles, metallic complexes or other semiconductor nanomaterials is an important and interesting strategy to yield electronic coupled photocatalysts with improved performance in relation to overall photocatalytic activity, stability and visible light absorption capacity [21,22].

Ferric hexacyanoferrate ($Fe_4[Fe(CN_6)]_3$), commonly known as Prussian Blue (PB), is one of the oldest synthetic metal coordination compounds and the main member of an archetypical class of cyanometallates solid-state frameworks (Prussian Blue Analogues) [23,24]. Prussian Blue is a mixed-valence compound in which the simultaneous occurrence of both nitrogen-coordinated high-spin Fe(III) sites and carbon-coordinated low-spin Fe(II) sites results in unique electronic, catalytic and magnetic properties [23–27]. TiO_2-PB nanocomposites prepared by chemical, photochemical and electrochemical methods were previously reported by different authors [28–30], the obtained materials being mostly explored for electrochemical applications but also as photoactive materials [31–35]. The photoactive behavior of such systems is based on the photo-induced electron transfer from the semiconductor titania particle towards the deposited PB layer. Upon UV excitation, the photoexcited electrons accumulated in the CB of titania have enough redox potential to reduce PB into its reduced form (Prussian White (PW)). Reduction of high-spin Fe(III) sites leads to color bleaching and change in magnetic susceptibility of PB layer, thus yielding photochromic and photomagnetic properties. Additionally, *in-situ* generated PW species may catalytically reduce adsorbed species such as metal ions and organic molecules, as demonstrated by electroanalytical studies employing PB-modified electrodes [36,37].

Based on the above-mentioned previous reports, in this study, we propose to use PB as a co-catalyst for the enhanced Cr (VI) photocatalytic reduction promoted by TiO_2 and SiO_2/TiO_2-based photocatalysts. Even though TiO_2-PB was previously explored in photoactivity-based applications (photovoltaic, photochromic and photomagnetic materials), the photocatalytic activity of TiO_2-PB system has remained understudied. To the best of our knowledge, there is only one report on the use of TiO_2-PB as a heterogeneous photo-Fenton catalyst [33] and no studies detailing the intrinsic photocatalytic activity of the material towards removal of water contaminants. Different TiO_2-based materials were used in this study: (i) conventional TiO_2 nanoparticles, (ii) silica-supported small anatase TiO_2 (SiO_2@TiO_2 core@shell) particles, (iii) TiO_2 aerogel particles and (iv) two different silica-titania aerogels (SiO_2@TiO_2 core@shell aerogels and SiO_2-TiO_2 mixed aerogels). Thus, the main objective of the present study was to explore the role of PB as a co-catalyst in improving the photoreduction performance of the different TiO_2-based materials mentioned above and to find the best photocatalytic system for Cr(VI) removal from water under practically feasible conditions.

2. Experimental

2.1. Reagents

Titanium (IV) dioxide anatase nanoparticles (TiO_2-A, 99.9%, Sigma-Aldrich), titanium (IV) tetrachloride ($TiCl_4$, 99%, Sigma-Aldrich), titanium (IV) isopropoxide (TiP, 97%, Sigma-Aldrich), tetraethylortosilicate (TEOS,

98% Sigma-Aldrich), potassium hexacyanoferrate(III) ($K_3Fe(CN)_6$, 99%, Sigma-Aldrich), iron (III) nitrate nonahydrate ($Fe(NO_3)_3.9H_2O$, 99%, Sigma-Aldrich), potassium dichromate ($K_2Cr_2O_7$, 99%, Synth), 1,5-diphenyl carbazide (DPC, 99% VETEC), propylene oxide (PO, 99% Sigma-Aldrich), ammonium hydroxide (NH_4OH, 28%, Sigma-Aldrich), potassium bromide (KBr, spectroscopic grade, Sigma-Aldrich), N,N-dimethylformamide (DMF, anhydrous, Sigma-Aldrich), isopropanol (HPCL grade, Panreac), absolute ethanol (HPCL grade, Panreac), hydrochloric acid (HCl, 37%, QHEMIS), nitric acid (HNO_3, 35%, QHEMIS) and sulfuric acid (H_2SO_4, 98%, QHEMIS) were purchased from respective suppliers and used without further purification. For reader´s convenience, a Table (Table S1) summarizing the sample codes and abbreviation used for the reagents is provided in the supplementary material.

2.2. Preparation of SiO_2-TiO_2 particles and aerogels photocatalysts

Silica-titania particles and aerogel photocatalysts were prepared based on sol-gel methodologies previously developed and reported by our group [38,39]. The SiO_2@TiO_2 core@shell particles (denoted as ST, henceforth) were synthesized by deposition of TiO_2 on Stober silica (SiO_2) spheres by solvent-controlled hydrolysis of TiP as alkoxide precursor. The method involves pre-adsorption of TiP on SiO_2 sphere from a mixed alcohol solvent (1:3 isopropanol: ethanol) followed by dropwise addition of water-solvent mixture to complete the hydrolysis of TiP and allowing condensation of the hydrolyzed products on the surface of SiO_2 particles. The amorphous titania in these ST samples was crystallized using hydrothermal treatment (110 °C, 24h) in a homemade Teflon-lined brass hydrothermal reactor. The ST samples were dried at 60 °C for 24h and annealed at 600 °C for 1h (heating rate = 15 °C/min) to further increase titania crystallinity. Further details can be found in our earlier studies [38,40].

A $TiCl_4$–based sol-gel route was used to prepare nanostructured SiO_2@TiO_2 core@shell aerogels (denoted as ST-TID) and SiO_2-TiO_2 mixed silica-titania aerogels (denoted as ST-EAG), employing a $TiCl_4$/DMF solution as the precursor solution. The ST-TID were prepared by thermo-induced deposition (TID) method. To prepare ST-TID aerogels, SiO_2 wet gels were soaked in $TiCl_4$/DMF precursor solutions containing trace amount of H_2O for 24 h and subsequently heated at 80 °C for 24 h in an oven to achieve thermolytic deposition of TiO_2 on SiO_2 and thus obtain ST-TID wet-gels. The ST-EAG gels were prepared by the epoxide-assisted gelation (EAG) method using the same $TiCl_4$/DMF precursor solutions, propylene oxide as the gelification agent and the pre-prepared SiO_2 aerogel powder as the silica source [39]. The SiO_2 aerogel powder was mixed with $TiCl_4$/DMF solution and, after 24 h of stirring, gelation was induced by the addition of a DMF/propylene oxide mixture to obtained ST-EAG wet-gels. TiO_2 wet gel (TiO_2-EAG) were prepared by a similar procedure without the addition of SiO_2 aerogel particles. After their preparation, the obtained wet gels (ST-TID, ST-EAG and TiO_2-EAG) were aged for 24 h at room temperature, washed once with DMF and several times with ethanol and acetone before being converted into dry aerogels by CO_2 supercritical drying (P= 1500 psi, T= 50 °C). The obtained aerogel

monoliths were ground into fine powders and calcined at 600 °C. The details of synthesis of aerogel samples have been reported elsewhere [39].

2.3. Photocatalysts modification with Prussian Blue (PB)

A photo-assisted deposition method [30] was used to deposit PB (ferric hexacyanoferrate, $Fe_4[Fe(CN_6)]_3$) on the surface of different photocatalysts (TiO_2-A, TiO_2-EAG, ST, ST-TID and ST-EAG) particles or aerogels. For this purpose, 125 mg of the photocatalyst powder were dispersed in 100 mL of an aqueous suspension of $K_3[Fe(CN)_6]$ by sonication and the mixture was kept under magnetic stirring for 4 h. The mixture was then transferred to double-jacket borosilicate reactor (maintained at 22 °C through water circulating in the outer part) and 50 mL acidified $Fe(NO_3)_3$ solution (prepared in 0.1 mol.L^{-1} HNO_3) was drop-wise added to the reactor while being continuously illuminated with UV light from a 150W Xe/Hg lamp (LightningCure, Hamamatsu, Japan) placed a distance of 9 cm from the reactor (Fig. 1b). After 1h of continuous irradiation, the resulting blue color suspension was centrifuged to separate PB-modified photocatalysts particles. The precipitates thus obtained were washed once with dilute HNO_3 (0.1 mol.L^{-1}) and twice with deionized water and then dried in an oven at 70 °C. The molar concentrations of $K_3[Fe(CN)_6]$ and $Fe(NO_3)_3$ were varied to deposit different amounts of PB on the surface of photocatalysts (Table 1).

2.4. Characterization techniques

X-ray diffractograms (2θ range = 10–80°, step = 0.020°) of the samples were obtained using a D8 advance diffractometer (Bruker, Germany), operated at 40 mA and 40 V and employing Ni-filtered Cu Kα X-ray (0.154 nm) radiation. FTIR spectra (4000–400 cm^{-1}, resolution 4 cm^{-1}) of the samples (3 mg sample + 100 mg KBr) pressed into pellets were collected using an IRAffinity-1S spectrophotometer (Shimadzu, Japan). Raman spectra were obtained using a Nicolet Almega Confocal Raman spectrometer coupled to an Olympus microscope (Thermo Fisher Scientific, USA). The spectra were collected using HeNe laser (λ = 632.8 nm) operated at 13% intensity as a source of excitation, accumulating 16 scans with a 10 s collection time. Scanning electron microscopy (FEG-SEM) images of the samples deposited on monocrystalline silicon substrates and sputter-coated with a thin (~ 6 nm) gold layer were obtained using an Inspect F-50 (FEI, Netherland) microscope, equipped with an Everhart–Thornley SE detector and a field emission gun (FEG) and operating at 5 kV electron beam accelerating voltage. Samples for transmission electron microscopy (TEM) analysis were deposited from a dilute suspension onto copper-coated copper minigrids (CFC-200Cu, EMS, USA) and analyzed using a Philips CM-200 Super Twin (FEI,, USA) microscope operating at a maximum acceleration voltage of 200 kV. X-Ray fluorescence (XRF) spectroscopy was employed for a semi-quantitative elemental analysis of the sample using the standardless analysis package Omnian (PANalytical, Netherlands). The XRF measurements (acquisition

time 840 s) were performed on benchmark MiniPal4 (PANalytical, Netherlands) energy-dispersive spectrometer equipped with a rhodium tube as X-ray source. Nitrogen (N_2) physisorption measurements were performed on an ASAP 2010 Micromeritics equipment (Micromeritics, USA). For these measurements, the samples were heated at 120 °C for 12 hours to remove adsorbed water. Specific surface area (S_{BET}) was determined from the adsorption/desorption isotherms using the Brunauer–Emmett–Teller (BET) method, total pore volume (V_p) as the volume of nitrogen adsorbed at a point close to the nitrogen saturation pressure and average pore size (l_p) as $l_p = 4V_p/S_{BET}$. Pore size distribution (PSD) analysis was carried out using DFT Plus Micromeritics software based on the classical Kelvin equation and the Harkins and Jura isotherm model for cylindrical pores [41,42].

2.5. Photocatalytic reduction of hexavalent chromium (Cr(VI))

The photo-reduction reaction of Cr(VI) was used to evaluate the photo-reducing capacity of the photocatalysts before and after modification with PB. For this purpose, 35 mg of the photocatalyst was dispersed in 35 mL water by sonication and then mixed with 35 mL of $K_2Cr_2O_7$ solution (containing 20 $mg.L^{-1}$ of Cr (VI)). The photocatalysts/ $K_2Cr_2O_7$ mixture was allowed to stir in dark for 30 min and then illuminated with UV light from the Xe/Hg lamp mentioned earlier. Sample aliquots were withdrawn at 10 min interval, centrifuged (to separate the photocatalyst particle) and the concentration of Cr(VI) in the supernatant layer was monitored spectrophotometrically. For this purpose, Cr(VI) was first converted to a colored specie (λ_{max}= 542 nm) employing 1,5 diphenylcarbazide (DPC) as a complexing agent [43]. For this purpose, 200 µL of the sample (supernatant part) were added to a solution containing H_2O (1 mL), 1,5 diphenylcarbazide solution (0.2 mL of 0.5 g/L solution in acetone) and H_2SO_4 (0.1 mL) which led to the immediate formation of a pinkish solution the intensity of which depends on the amount of Cr(VI) present in the sample. The absorbance of this complex at 542 nm was monitored using a UV-visible spectrophotometer.

3.1 Results and Discussion

3.1. Modification of photocatalysts with Prussian blue (PB) co-catalyst

The photocatalysts nanoparticles (TiO_2-A, ST) and aerogels (TiO_2-EAG, ST-TID, ST-EAG) were surface-modified with PB using the photodeposition methodology developed by Tada and co-workers [30]. This method employs $[Fe(CN)_6]^{3-}$ and an Fe^{3+} salt as molecular precursors and is based on the fact that photo-excited electrons in the conduction band (CB) of TiO_2 are capable of reducing $[Fe(CN)_6]^{3-}$ to $[Fe(CN)_6]^{4-}$. In the presence of Fe^{3+} cations, the resulting reduced specie triggers PB nucleation/growth selectively on the surface TiO_2 particles. Fig. 1a illustrates the process and reactions involved in PB photodeposition on TiO_2-based materials. During PB photodeposition on the surface of photocatalyst samples, we observed a noticeable color change of the reaction mixture from yellow (color of $[Fe(CN)_6]^{3-}$ precursor) to green and finally to intense blue (Fig. 1b),

indicating successful deposition of PB on these materials. The formation of PB was confirmed by vibrational spectroscopy and its % loading was determined by XRF analysis.

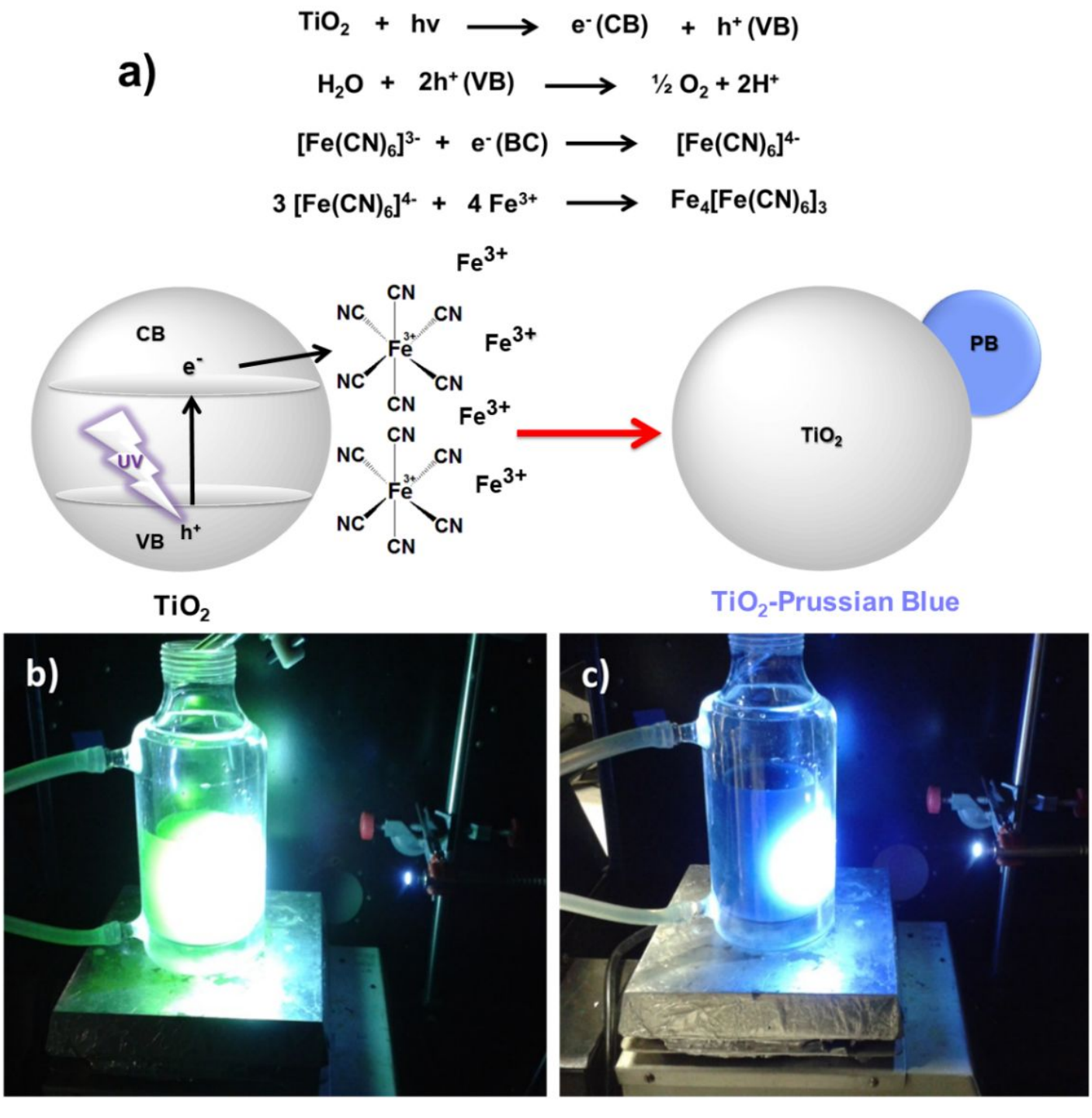

Figure 1. (a) Illustrative scheme and reactions involved in Prussian blue photodeposition process on the surface of titania-based photocatalysts. Digital photographs showing PB photodeposition on SiO_2@TiO_2 particles as noticed from a color change from (b) light yellow (before illumination) to (c) intense blue (after illumination for 1h)

3.1.1 X-ray Fluorescence analysis (% TiO_2 and Fe loading)

As mentioned earlier, the amounts of iron-based precursors ($K_3[Fe(CN)_6]$ and $Fe(NO_3)_3$) added in the reaction mixture were varied to photodeposit different amounts of PB on the surface of photocatalysts (Table 1). Resultantly, a notable change in coloration was observed in these different samples, with the final blue color progressively becoming more intense with the increase in PB precursors' concentration (inset Fig. 2). XRF analysis was employed to quantify the PB (%Fe) and TiO_2 contents of each sample (Table 1). Importantly, an almost linear correlation between %Fe loading (determined by XRF) of the samples (ST-PB series) and the total molar amount of Fe-based precursors added in the photodeposition step (Figure 2) confirms the effectiveness of the photodeposition process and that the PB loading of the samples can be easily tuned by simply changing the precursors concentration while keeping the UV irradiation time fixed. Moreover, it is worth noting that for a given irradiation time (1h) and precursors concentration, the %Fe loading of different TiO_2-materials used in this work is quite similar (3–3.7%). These results suggest that the amount photodeposited PB does not vary significantly with type or chemical composition of titania or silica-titania based photocatalysts despite the fact that they show quite different textural and photocatalytic properties [38,39].

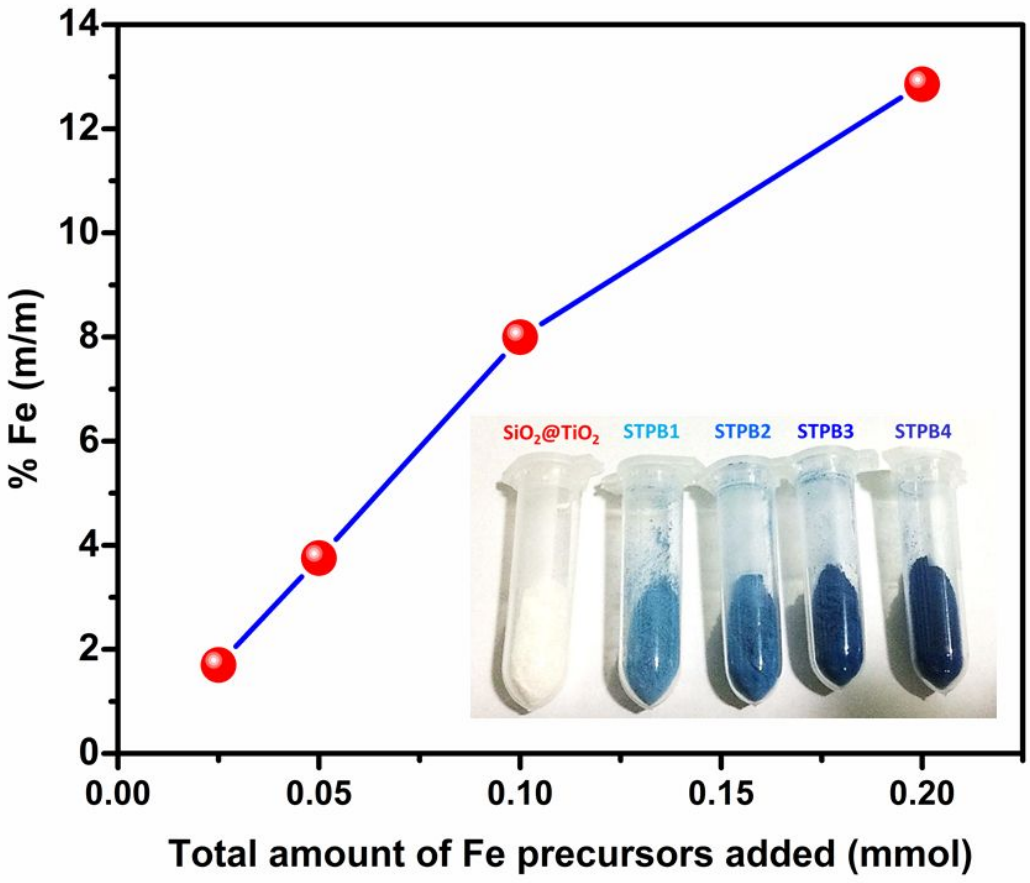

Figure 2. Variation of %Fe determined by XRF analysis for SiO_2@TiO_2-PB samples (ST-PB series) as function of initial amount of iron-based precursors added during photodeposition process (total amount of Fe added in mmol). The inset shows digitals photographs of the corresponding samples.

Table 1. Summary of the prepared PB-modified TiO_2 and SiO_2-TiO_2 samples, showing their respective initial composition (%TiO_2 determined by XRF), amounts of iron-based precursors employed during photodeposition process and Fe loading (mass %) values determined by XRF analysis.

Sample	Base photocatalyst	Initial TiO_2 loading	$K_3[Fe(CN)_6]$ mmol	$Fe(NO_3)_3$ mmol	%Fe
ST-PB1	SiO_2@TiO_2 particles	21%	0.0125	0.0125	1.7%
ST-PB2	SiO_2@TiO_2 particles	21%	0.025	0.025	3.7%
ST-PB3	SiO_2@TiO_2 particles	21%	0.05	0.05	8.0 %
ST-PB4	SiO_2@TiO_2 particles	21%	0.1	0.1	12.8%
ST-EAG-PB2	EAG SiO_2-TiO_2 Aerogel	60%	0.025	0.025	3.0%
ST-EAG-PB3	EAG SiO_2-TiO_2 Aerogel	60%	0.05	0.05	6.9%
ST-TID-PB2	TID SiO_2@TiO_2 Aerogel	65%	0.025	0.025	3.6%
ST-TID-PB3	TID SiO_2@TiO_2 Aerogel	65%	0.05	0.05	6.2%
TiO_2-EAG-PB2	EAG TiO_2 Aerogel	100%	0.025	0.025	3.7%
TiO_2-EAG-PB3	EAG TiO_2 Aerogel	100%	0.05	0.05	7.9%
TiO_2-A-PB2	TiO_2 NPs Sigma-Aldrich	100%	0.025	0.025	3.2%
TiO_2-A-PB3	TiO_2 NPs Sigma-Aldrich	100%	0.05	0.05	6.0%

3.1.3 Molecular vibrational spectroscopy study (FTIR and Raman)

The formation of PB on the surface of the photocatalysts was confirmed by FTIR and Raman spectroscopy. Based on the assignment of the vibrational modes of PB analogues by Kettle et al [44], PB is expected to show three cyanide (C≡N) stretching vibrational modes, two of which are Raman-active (A_{1g} and E_g modes) and one infrared-active (T_{1u} mode). The FTIR spectrum of representative ST-PB sample indicates the presence of vibrational modes characteristics of SiO_2-TiO_2 composites [45], as identified in Fig.3a. The broad band around 3400 cm^{-1} (O–H stretching) may come from adsorbed water molecule or surface hydroxyl groups of SiO_2/TiO_2 material. Of greater relevance is the signature FTIR band of PB at around 2081 cm^{-1} which originates from the stretching of C≡N bonds (T_{1u} vibrational mode) present in cyanometallate extended network of PB. As expected, the intensity of this characteristic vibrational band of PB increases with the increase in PB content of the samples (inset, Fig. 3a).

The characteristic FTIR vibrational modes of cyanide ligands (normally occurring at 2040 cm^{-1} for isolated ferrocyanide ions) are quite sensitive towards coordination to metal centers and often shift to higher wavenumbers upon coordination of the ferrocyanide nitrogen terminations to metallic centers (as in

Fe(II)–C–N–M) [25]. Since the FTIR spectra of our PB-modified samples show the cyanide vibrational modes at high wavenumbers (2083–2077 cm^{-1}) (Figs. 3a.b), it confirms the formation of PB extended network formed by Fe(II)–C–N–Fe(III) bridging bonds. Moreover, the FTIR band positions observed in our samples are also consistent with the values reported for pure PB (2070 cm^{-1}) and TiO_2-PB composite (2088 cm^{-1}) [30,46]. The same vibrational mode (C≡N linkages) is Raman active and gives rise to a strong Raman band around 2150 cm^{-1} (totally symmetrical A_{1g} mode) with a shoulder around 2090 cm^{-1} (E_g mode) [25,44] in the Raman spectra of our SiO_2-TiO_2-PB materials (Fig. 3c) which further confirms the formation of PB in these samples.

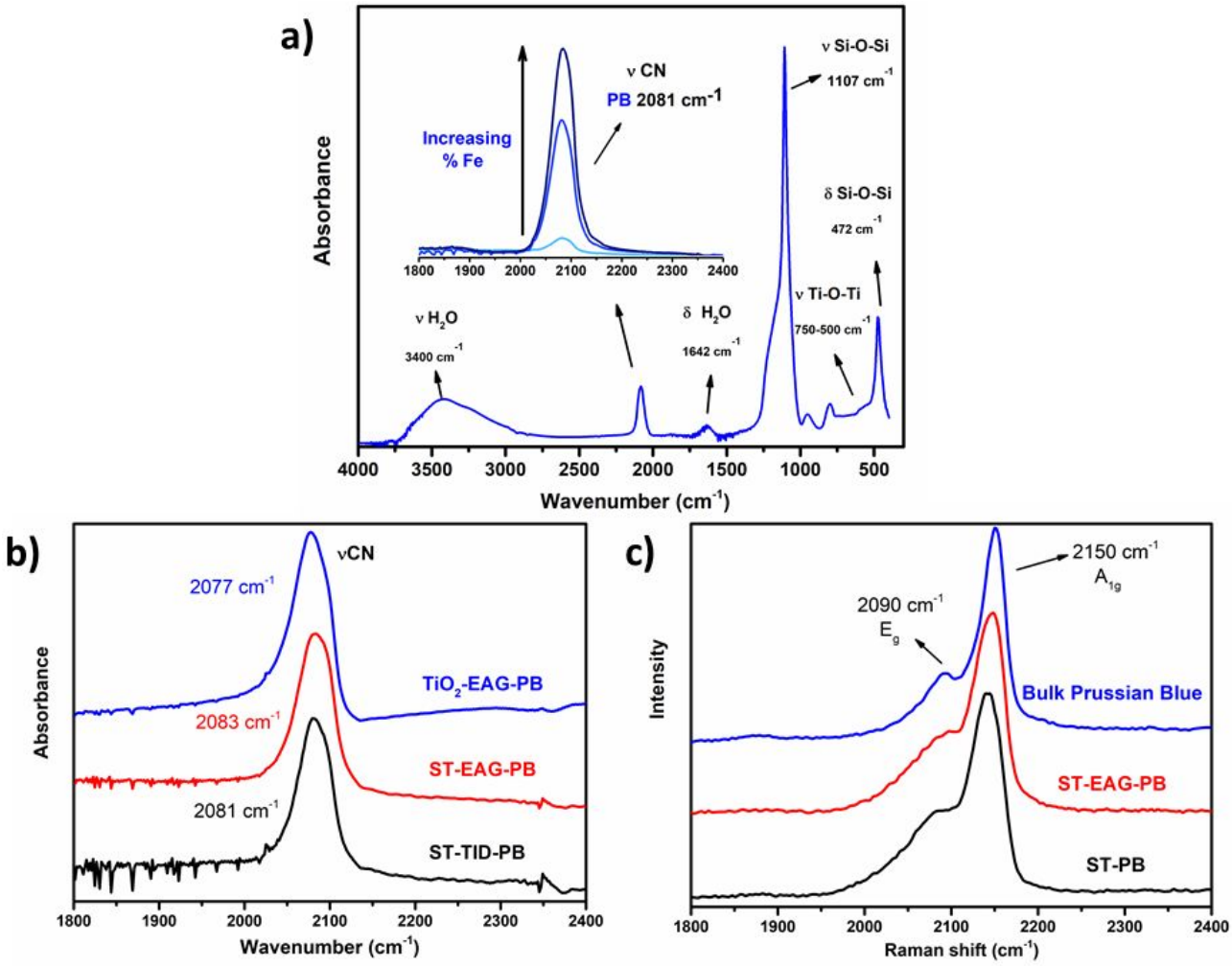

Figure 3. (a) Representative FTIR spectra of ST-PB sample. The inset shows the increase in intensity of C≡N stretching band as function of PB content of the samples. (b) The C≡N stretching vibration region for PB-modified titania and silica-titania aerogels (ST-TID-PB and ST-EAG-PB). (c) Raman spectra of PB-modified photocatalysts particles (ST-PB) and aerogels (ST-EAG-PB) as compred to the spectrum of pure bulk PB sample.

3.1.4 X-ray diffraction analysis

The formation of PB in different samples and its crystalline structure was studied using XRD analysis (Figure 4 and Figure S1). All samples exhibit the characteristics diffraction peaks of anatase except the pure

TiO_2 aerogels (TiO_2-EAG-PB) which also show additional diffraction peaks of rutile phase also (Figs. 4a). The broader feature centered around 22° corresponds to amorphous SiO_2 in these silica-titania samples. In addition to the characteristic diffraction peaks of TiO_2, additional diffraction peaks (marked with *) are observed in diffractograms of all samples (except STPB-1 which has the lowest Fe concentration, see Figure S1) at 2θ values of 17.8°, 35.4° and 39.8°, which are attributed to the (200), (400) and (420) planes of the fcc crystalline structure of PB [47]. The absence of these characteristic diffraction peaks of PB in ST-PB1 samples may be related to PB loading below the limit of detection of the technique.

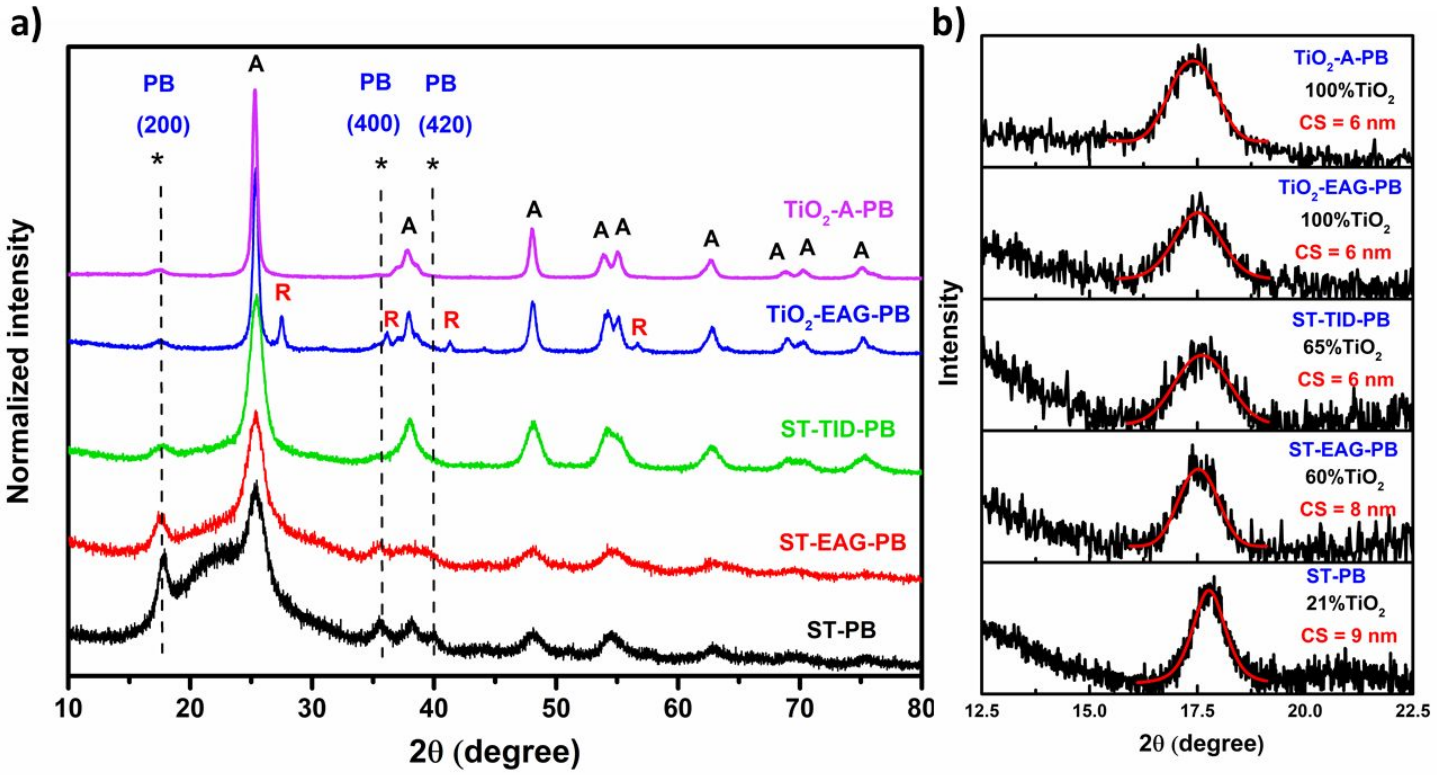

Figure 4. a) X-ray diffractograms of silica-titania and pure titania photocatalysts containing similar amounts of PB; (b) X-ray diffraction peaks corresponding to the crystalline plane (200) of the photodeposited PB in the different samples. For a better visualization of the diffraction peak and measurement of the crystallite size (CS) of the photodeposited PB, a baseline correction and peaks fitting were performed using the Pseudo-Voigt function (red curves in (b)).

Diffraction peaks intense enough to allow calculation of the crystallite size (CS) of PB were observed only in samples with higher (> 6% Fe) PB loading (PB3-series) (Fig. 4b). The crystallite sizes calculated based on the width of the (200) diffraction plane of PB using Scherrer formula varied between 6 and 9 nm, indicating the nanocrystalline nature of the photodeposited PB. A slight decrease in PB crystallite size with increase in %TiO_2 loading of the samples was observed (Fig. 4b). This behavior may be related to the high affinity of the titania surface for the $[Fe(CN)_6]^{-4}$ ions which bind to the surface of TiO_2-based materials by chemisorption involving Ti(IV)–CN–Fe(II) bridging bonds [48]. This chemisorption process may promote greater dispersion of these adsorbed species (which act as nucleation sites for the formation of PB nanocrystallites) on the surface of TiO_2.

A higher TiO_2 content of the silica-titania materials is then expected to result in a greater number of nucleation sites of the PB, leading to a decrease in the final crystallites size at the end of photodeposition process.

3.1.5 Morphological study using electron microscopy (FEG-SEM and TEM analysis)

Among the TiO_2-based photocatalysts studied in this work, the SiO_2@TiO_2 core@shell particles (ST series) have the most regular and uniform morphology. These particles were thus selected to evaluate the effect of PB deposition on the microstructure and morphology of the photocatalysts and to verify if PB is essentially deposited on their surfaces. Figs. 5 and 6 compare the FEG-SEM and TEM micrographs, respectively, of a representative ST sample before and after photodeposition of PB. An analysis of the SEM images of ST and ST-PB2 samples indicates that both materials have a similar morphology, with only a subtle change in morphology induced by the incorporation of PB (Figs. 5a,b).

It is important to note that no free or isolated PB nanoparticles can be seen in these images, suggesting that PB is essentially and selectively deposited on the surface of the photocatalysts by heterogeneous nucleation and no precipitation as a result of homogenous nucleation in solution occurs. A closer look at the higher magnification FEG-SEM images (Figs. 5c and 5d) indicates that the surface texture of the particles undergoes a slight change after the photodeposition process, with the PB-modified particles (ST-PB2) appearing to be somewhat smoother and slightly bigger than unmodified ST particles.

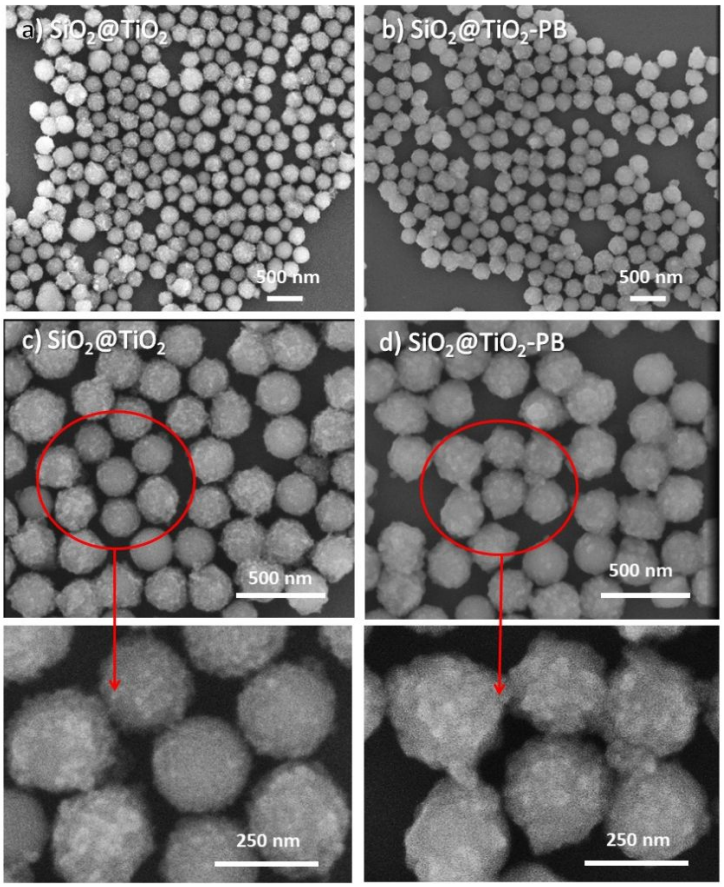

Figure 5. FEG-SEM images of (a,c) pristine ST core@shell particles in low (a) and higher (c) magnification, and (b,d) PB-modified sample (ST-PB2) in low (b) and high magnification (d). The bottom part of the Figure shows the magnified views of the encircled regions of each sample.

The TEM images of ST particles clearly indicates the formation of a TiO_2 shell consisting of small nanoparticles around SiO_2 sub-micron particles, resulting in a core@shell structure. A comparison of the TEM macrographs of ST and ST-PB3 samples (Fig. 6) reveals that the shell part of ST core@shell particles becomes denser and thicker after modification with PB and the individual titania nanoparticles observable in ST sample (Figs. 6a,c) are less visible in ST-PB3 sample (Figs. 6b,d). This is probably due to the formation of a second PB layer around the titania nanocrystals in the shell part of ST particles, leading to the formation of SiO_2@TiO_2@PB core@shell@shell architecture. Previous studies on TiO_2-PB composites have also suggested that PB tends to deposit itself in the form of thin layers on the surface of titania particles [28,30]. The higher magnification TEM images (Figs. 6d,e) appear to show the formation of such a PB overlay on the surface of the ST particles. Finally, the EDS microanalysis indicated the presence of Fe, Ti and Si in these PB-modified ST particles (ST-PB3), further confirming the successful deposition of PB on the surface of ST core@shell particles.

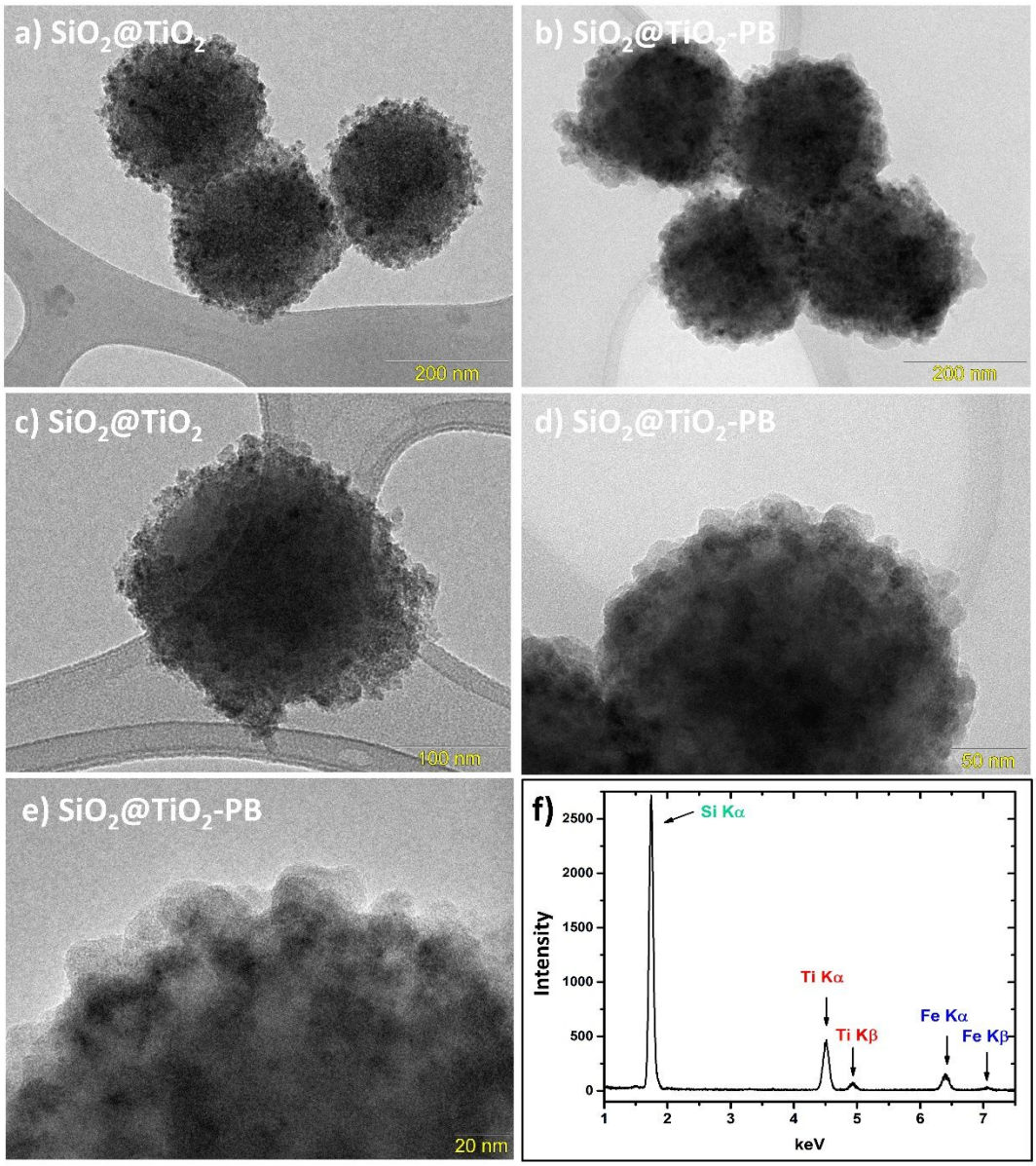

Figure 6. TEM images of (a,c) pristine ST core-shell particles in low (a) and higher (c) magnification, and (b,d,e) PB-modified sample (ST-PB3) in low (b) and higher magnification (d,e); (f) The EDS spectrum of the same ST-PB3 sample.

3.1.6 N_2 adsorption

The N_2 adsorption-desorption isotherms and pore size distribution (PSD) of SiO_2@TiO_2 core@shell particles (ST series), TiO_2 anatase nanoparticles, silica-titania aerogels (ST-TID and ST-EAG) and titania aerogels (TiO_2-EAG) are shown in Fig. 7 and the corresponding textural properties determined using BET method are summarized in Table 2. The N_2 adsorption isotherms of unmodified and PB-modified nanoparticles (ST and TiO2-A series) can be classified as type IV according to the general IUPAC classification [41], which are characteristic of the mesoporous materials. It thus suggests that the mesoporous nature of TiO2 shell (ST series) materials are maintained even after photodeposition of PB. The desorption isotherms obtained for ST, ST-PB , TiO_2-A and TiO_2-A-PB samples have hysteresis loops that resemble that of type H4 and H3 [41], which characterize solids that consist of aggregates or agglomerates of particles forming slit-shaped pores, cones and/or parallel

plates whose sizes are uniform and nonuniform, respectively. The photodeposition of PB on the surface of these materials generally leads to a slight increase in S_{BET} and V_p and a slight and irregular decrease in the I_p. This can be attributed to the formation of a second PB thin layer around the titania nanocrystals in the shell part of ST particle as discussed above in TEM analysis. This is corroborated with the PSD curves that show an increase in the incremental pore volume and the appearance of new pore classes in the mesoporous region (~20 nm) related to TiO_2 shell in SiO_2@TiO_2 particles.

Different textural properties of the TiO_2-EAG series and between two different silica-titania aerogels imply slightly different deposition of PB in the networks that compose these materials. As shown in Fig. 7b, the N_2 adsorption curves of silica-titania aerogels (ST-TID and ST-EAG series) and titania aerogels (TiO_2-EAG), both before and after PB deposition, can be classified as type IV isotherms [41], confirming that the mesoporous nature of the aerogels is preserved after surface modification with PB. The N_2 desorption curves obtained for ST-TID, ST-TID-PB2, TiO_2-EAG and TiO_2-EAG-PB2 aerogels can be classified as a type H1, suggesting the presence of uniform cylindrical mesopores formed by aggregates and or clusters of spheroidal particles [41]. Desorption isotherms for the ST-EAG series sample depict H3 type hysteresis characteristic of non-uniform slit-shaped pores [41,42]. The specific surface area value for TiO_2-EAG sample increase slightly after photodeposition of PB, while those of V_p and I_p decreases, probably because the thin layer of PB is formed on solid TiO_2 network filling the mesopores that make up the material. This effect can be observed in the PSD curves (Fig. 7b) as the incorporation of PB in the structure of TiO_2-EAG aerogels shift the PSD toward the mesopores, giving rise to new classes of pores. ST-TID and ST-EAG aerogels series shown the typical values of S_{BET}, V_p and I_p [39]. Nevertheless, slight differences in structural parameters are observed between the two different silica-titania aerogels after photodeposition of PB. For instance, while the porosity and average pore size increase for both materials after PB deposition, the S_{BET} decreases and increases for ST-EAG-PB2 and ST-TID-PB2, respectively. This discrepancy could be explained on the basis of the observation that the conventional nitrogen adsorption method can seriously underestimate the macropores region. Such inference is further supported by PSD analysis of the ST-TID and ST-EAG aerogels which shown the multimodal pore distribution on the mesopore and macropore regions (Fig. 7b). The PSD curves of the silica-titania aerogels shift toward the mesopore region after surface modification with PB, suggesting that overall photodeposition process results in a significant changes in the porosity of silica-titania networks.

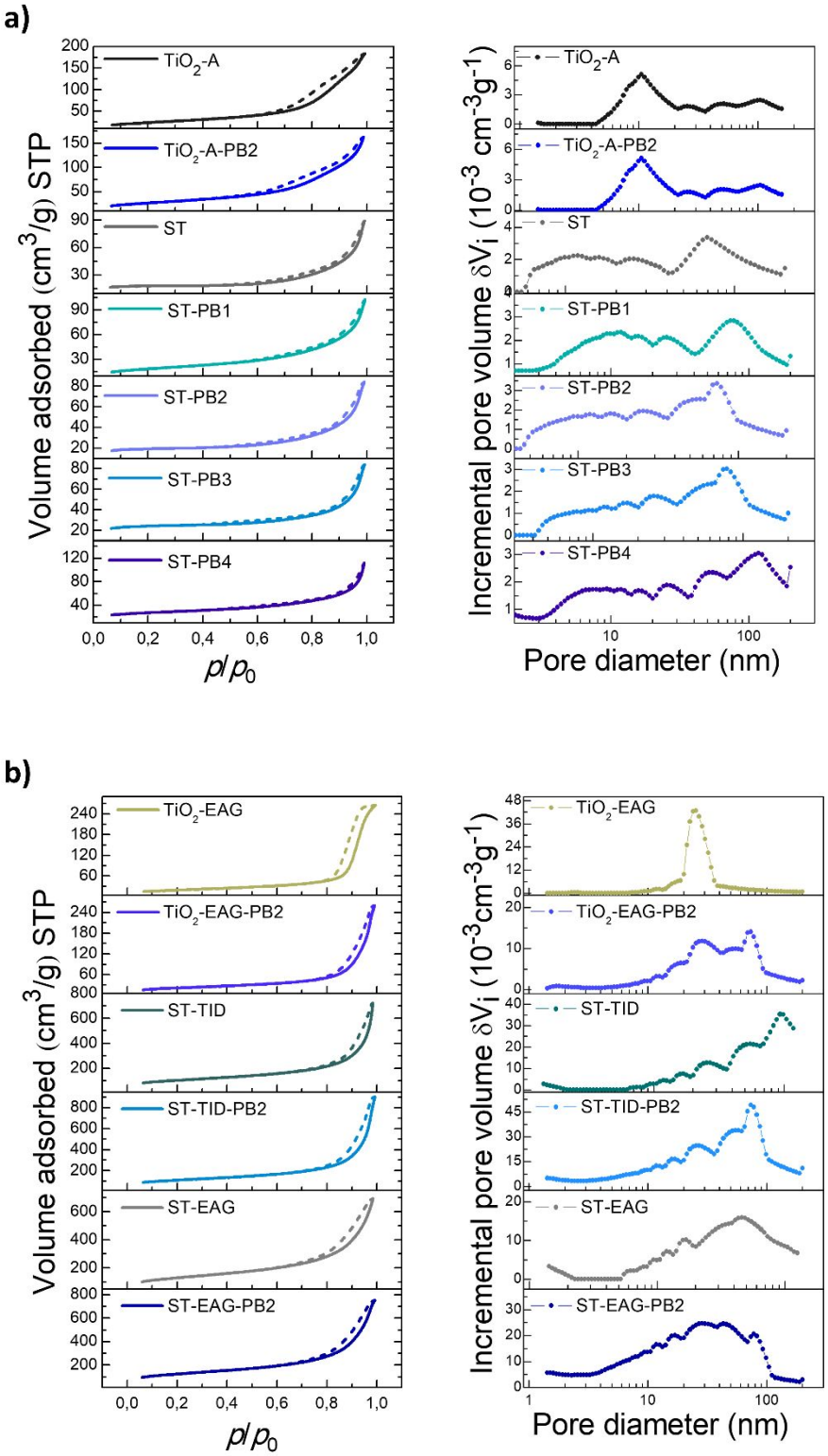

Figure 7. N_2 adsorption-desorption isotherms and pore size distribution (PSD) of (a) ST, ST-PB samples with different PB loadings, TiO_2 and TiO_2-PB particles and (b) different silica-titania and titania aerogels before and after modification with similar amounts of PB.

Table 2. Textural parameters (BET surface area, S_{BET}, pore volume, V_p and pore length l_p) obtained from N_2 adsorption and BET method for the ST series, TiO_2 particles, different silica-titania aerogels and titania aerogels.

Sample	S_{BET} ($m^2.g^{-1}$)	V_p ($cm^3.g^{-1}$)	l_p (nm)
ST	62	0.12	7.9
ST-PB1	66	0.14	8.6
ST-PB2	66	0.12	7.2
ST-PB3	83	0.12	5.7
ST-PB4	94	0.15	6.3
ST-EAG	465	1.04	8.9
ST-EAG-PB2	446	1.12	10.1
ST-TID	369	0.97	10.6
ST-TID-PB2	391	1.22	12.5
TiO_2-EAG	70	0.41	23.6
TiO_2-EAG-PB2	78	0.36	18.6
TiO_2-A	86	0.27	12.4
TiO_2-A-PB2	96	0.23	9.7

3.2. Cr (VI) photocatalytic reduction

The photocatalytic reduction of Cr(VI) to Cr(III) in the presence of different silica-titania and PB-modified silica-titania photocatalysts (ST and STPB samples) was carried out to evaluate the role of PB in the photocatalytic activity of these samples. Importantly, no solution pH adjustment was employed during the photocatalytic tests and the tests were carried out at natural unadjusted pH of around 5.6. The decrease in concentration of Cr(VI) was monitored by measuring the change in absorbance ($\lambda_{max.}$ = 545 nm) of Cr(VI)-DPC complex (see the digital photos in inset of Fig. 8a, also) as a function of UV illumination time (Fig. 8a). Figs. 8b and 8c compare the kinetic profiles and photocatalytic Cr(VI) reduction efficiency after 60 min of UV irradiation, respectively, for ST and ST-PB samples containing different amounts of PB. The Cr(VI) photoreduction efficiency of unmodified ST is low and this samples could reduce only 31±5% of Cr(VI) within 1h of UV illumination, as compared to 65–85% reduction observed in case of PB-modified ST-PB samples. It also worth mentioning that both the unmodified and PB-modified materials show low adsorptive removal efficiency (less than 10% Cr(VI) removal in the initial 30 min kept) under the dark conditions (Fig.S2 in supplementary material). These results thus confirm that the increased Cr(VI) removal performance of the PB-modified material is not related to the possible improved dark adsorption but to the photocatalytic processes taking place on the surface of the photocatalysts.

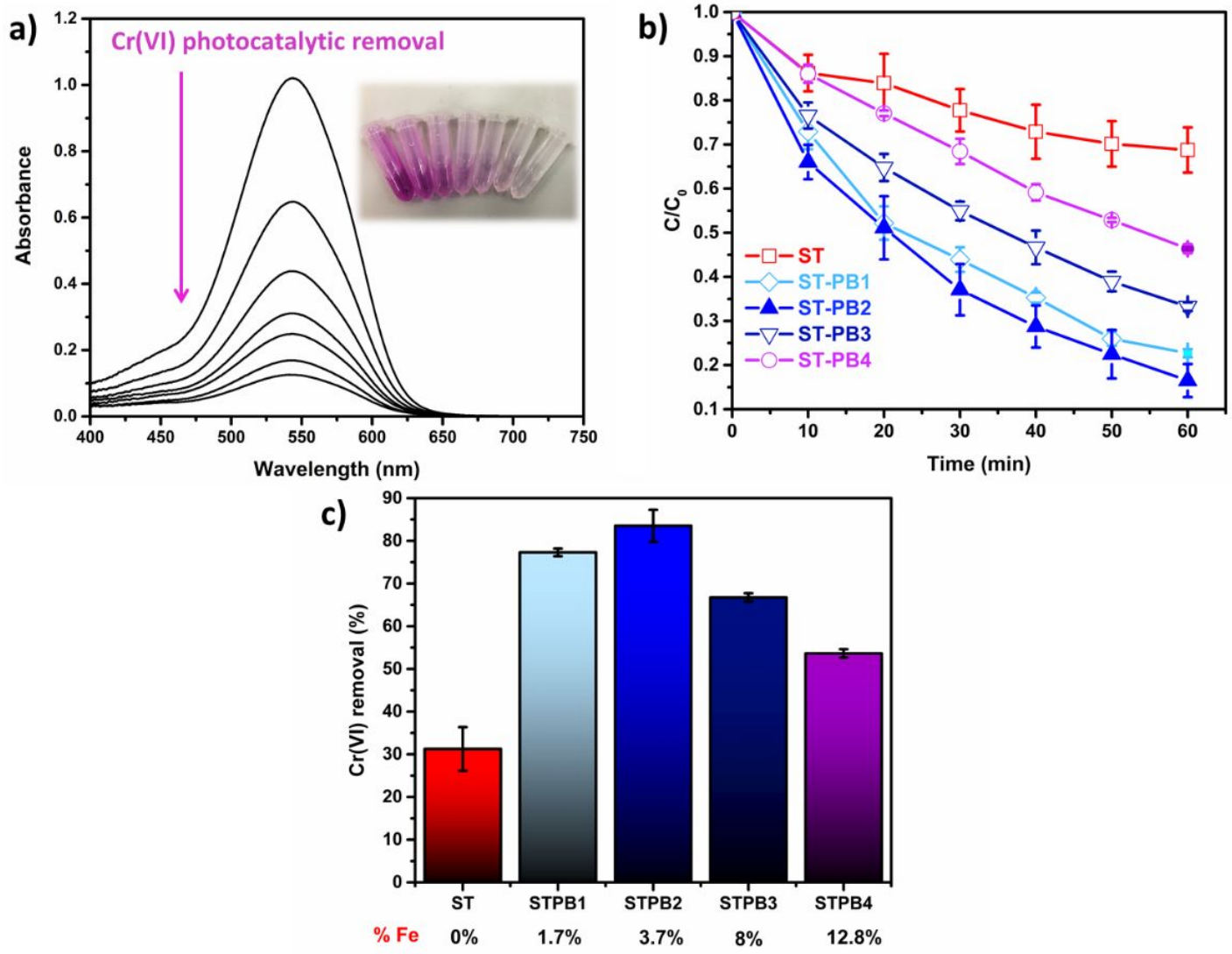

Figure 8. (a) Visible absorption spectrum of Cr(VI)-DPC complex showing the decrease in Cr(VI) content of the reaction mixture as a function of UV illumination time due to photocatalytic reduction of Cr(VI) to Cr(III) on the surface of SiO_2@TiO_2-PB particles (ST-PB2 sample); A comparison of the (b) kinetic profiles and (c) photocatalytic Cr(VI) reduction efficiency of unmodified (ST) and PB-modified ST samples (ST-PB series). The inset in **a** are digital photos of Cr(VI)-DPC complex obtained after different UV illumination intervals in the presence of ST-PB2 photocatalysts. Conditions: Cr(VI) = 10 mg. L^{-1}, pH = 5.6 (unadjusted).

Previous studies of Cr(VI) photoreduction by unmodified TiO_2 and other semiconductors have also reported a low efficiency of the process [11,12,49] and there are several factors responsible for this. These studies demonstrate that the photocatalytic reduction of Cr(VI) to Cr(III) is less efficient and slow in deionized water (less acidic medium) and in the absence of organic species that can act as electron donors (or hole scavengers). In the absence of such easily oxidizable species, the other possible oxidation reaction, occurring concomitantly with Cr(VI) reduction, is the oxidation of water which is kinetically unfavorable and slow [12,49]. The Cr(VI) reduction reaction is much more efficient in acidic environment as it involves participation of a large number of protons on the reactant side, as shown below [11].

Acidic media: $2\ Cr_2O_7^{2-} + 16\ H^+ \rightarrow\ 4\ Cr^{3+} + 8\ H_2O + 3\ O_2$

Neutral media: $4\ CrO_4^{2-} + 20\ H^+ \rightarrow 4\ Cr^{3+} + 10\ H_2O + 3\ O_2$

Moreover, the reduction potential of chromate ion decreases with decrease in the pH of the medium, making it a more oxidizing specie (more susceptible to reduction) in a more acidic medium [49,50]. Another factor that limits the efficiency of the photocatalytic reduction at higher pH values is the formation of $Cr(OH)_3$ as a product of the reduction reaction and its subsequent deposition on the surface of the photocatalysts, resulting in the progressive deactivation of the photocatalytic sites [51]. Considering the factors discussed above, it can thus be inferred that the efficiency of photoreduction of Cr(VI) using unmodified TiO_2 and SiO_2-TiO_2 materials is low, particularly in neutral or low acidic reaction media.

Modification of ST particles with PB leads to an enhancement of their photoreduction ability and higher Cr(VI) photoreduction efficiency (65–85%) was achieved for ST-PB samples (Figs. 8b,c). In general, all the PB-modified samples (ST-PB series) exhibit better photocatalytic activity as compared to unmodified ST particles (31±5%). Among the ST-PB series, ST-PB2 (3.7% Fe) shows the highest photoactivity, reducing 84±4% of Cr(VI) within 60 min of UV illumination, a value much superior than that achieved for unmodified ST (31±5%). Considering the PB loading in this sample as optimum, we then compared the photocatalytic activity of different SiO_2-TiO_2 and TiO_2 based aerogels and particles before and after modification with similar amount of PB (3–3.7% Fe) (Figs. 9,10 and S3). A general analysis of the results reveals that the unmodified SiO_2-TiO_2 and TiO_2 aerogels and particles show lower photocatalytic activity towards reduction of Cr (VI) (20–40% reduction) under the conditions employed and incorporation of PB in all of these samples leads to a significant improvement in the photocatalytic response (Fig. 9).

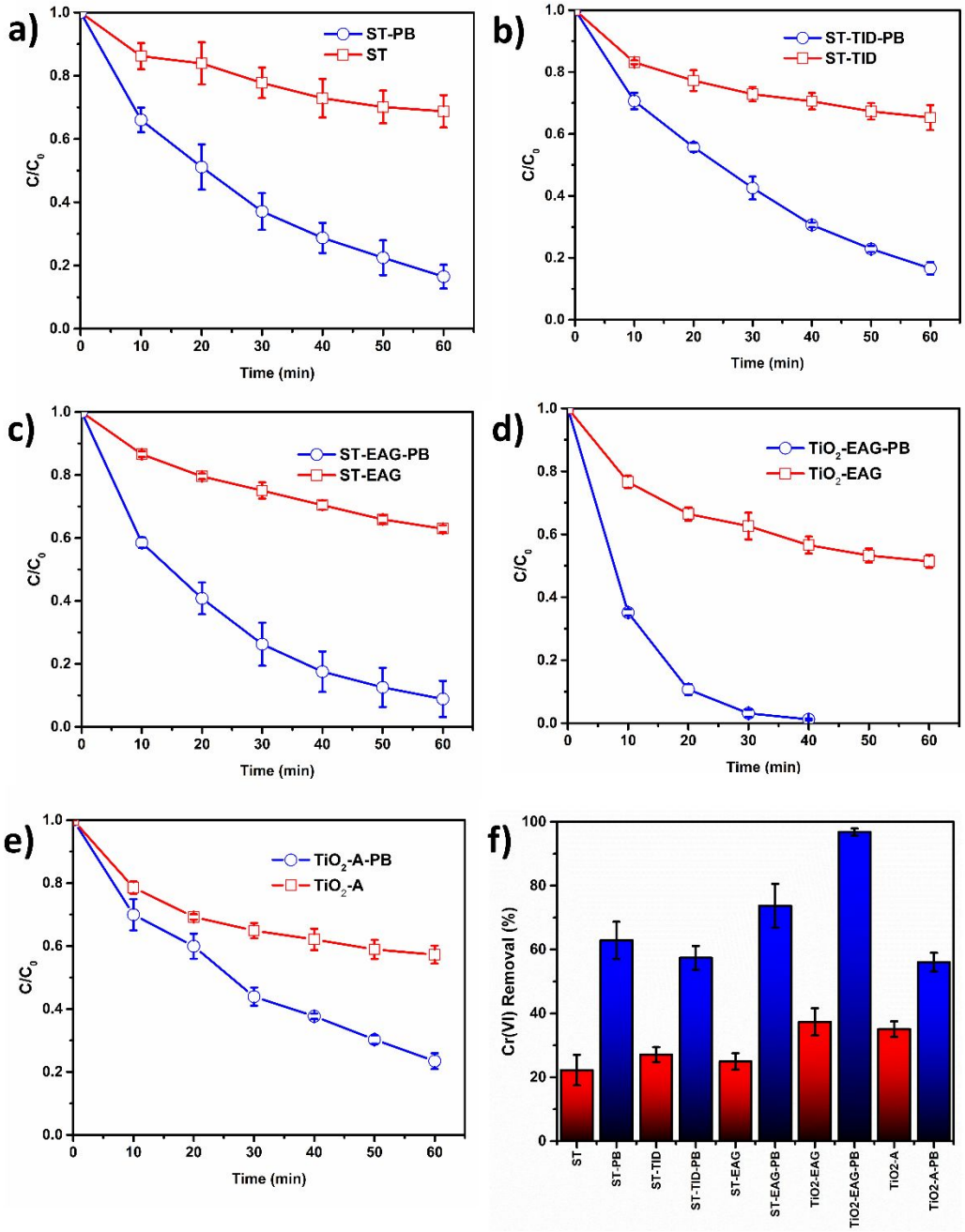

Figure 9. (a-d) Kinetic profiles showing a comparison of the photoactivity of titania and different silica-titania materials before and after modification with PB: (a) ST core@shell particles, (b) ST-TID Aerogel, (c) ST-EAG Aerogel, (d) TiO_2-EAG Aerogel, (e) TiO_2 anatase particles; (f) comparison of the Cr(VI) photoreduction efficiency after 30 min irradiation for different titania and silica-titania based photocatalysts with and without PB.

A comparison of the photocatalytic activity (Fig. 10a) and the first order kinetic constants (Fig. 10b) of different SiO_2-TiO_2-PB materials (particles and aerogels) modified with similar amount of PB reveals similar photocatalytic activity for these different samples. Interestingly, the highest photocatalytic activity was observed for titania aerogels modified with PB (TiO_2-EAG-PB2 sample) which could reduce 97±1% and 99±1% of Cr(VI) within 30 min (Figure 9f) and 40 min of UV irradiation (Figure S3), respectively, in deionized water and in the total absence of organic electron donors, a remarkable photocatalytic performance.

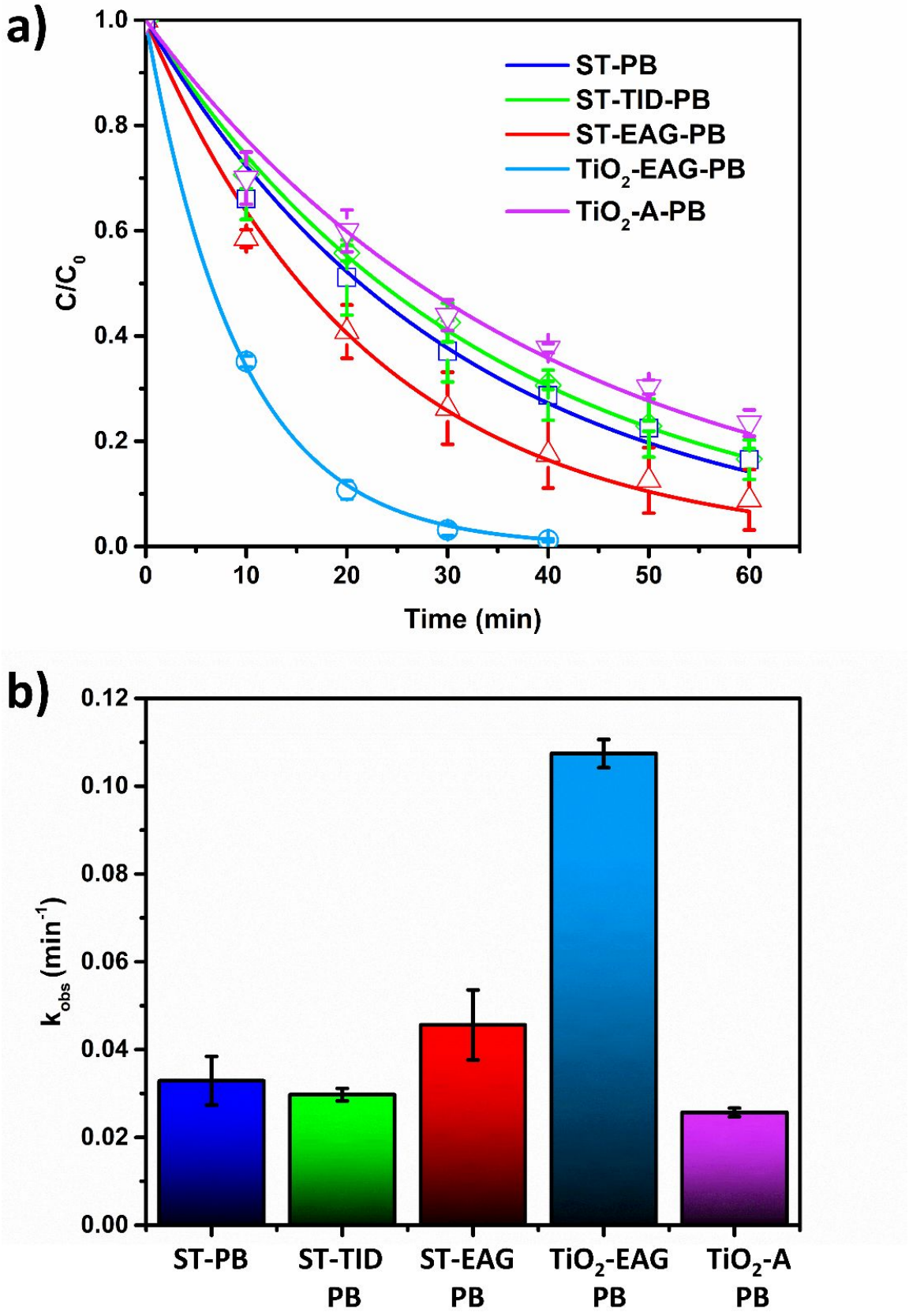

Figure 10. (a) Kinetic profiles and (b) first order kinetic constants for different SiO_2-TiO_2-PB2-type samples (particles and aerogels) modified with similar amount of PB (3–3.7% Fe).

Fig. 11 illustrates the proposed schemes to explain the improved photocatalytic activity of TiO_2-PB based photocatalysts. The superior photocatalytic activity of PB-modified samples can be attributed to the ability of the PB layer to act as an electron mediator between the titania surface and the Cr(VI) species in solution (Fig.11a). The transfer of electrons from the conduction band (CB) of TiO_2 to PB leads to the formation of its reduced form, the Prussian white (PW), by reducing Fe (III) high-spin sites [31,52]. These reduced sites can, in turn, act as catalytic sites for the reduction of Cr(VI) to Cr(III), with the efficiency of the process being increased as these high spin Fe (II) species have a lifetime longer than that of the photo-excited electrons in titania, thereby, increasing the probability of electrons transfer to the ions in solution. A previous research study, involving glassy carbon/PB electrode, has in fact proved the electrocatalytic activity of PB towards reduction of Cr (VI) and the authors explored this effect for the development of electroanalytical sensors for the selective detection of very low Cr (VI) concentrations [37]. It is also worth-mentioning that the efficient transfer of electrons from the CB of TiO_2 to the PB layer at the TiO_2-PB interface leads to an effective charge separation in TiO_2, thereby reducing surface recombination processes, and thus improving the photocatalytic efficiency of the material. To the best of our knowledge, this is the first report on the ability of PB to act as a co-catalyst in Cr(VI) photocatalytic reduction reactions promoted by semiconductor based catalysts. Finally, the greater photocatalytic performance shown uniquely by the TiO_2-EAG-PB sample suggests a possible synergistic effect resulting from the role of PB role as a co-catalyst and the occurrence of bicrystalline anatase/rutile heterojunctions, thus improving the charge separation efficiency in TiO_2 and hence the overall photocatalytic performance (see Fig. 11b). Such hypothesis is further reinforced by the contrasting photocatalytic performance of TiO_2-A and TiO_2-EAG samples upon modification with PB. Considering that both of these titania photocatalysts show quite similar specific surface area, crystallite size and photocatalytic behavior before modification, their only difference is the TiO_2 phase composition (pure anatase for TiO_2-A and anatase/rutile mixture for TiO_2-EAG). While PB-modified pure anatase titania shows a 1.85 times higher Cr(VI) photocatalytic reduction first-order kinetic constant compared to unmodified sample, TiO_2-EAG shows a 9 times increased kinetic constant value upon PB incorporation (see Figure S4), thus indicating the important role of titania phase composition on the overall efficiency of PB as a photocatalytic reduction co-catalyst.

In order to compare the Cr(IV) removal performance of the most photoactive samples (TiO_2-EAG-PB aerogel) with that of earlier reported high performance titania-based photocatalysts, we conducted additional photocatalytic Cr(VI) reduction tests (Fig. S5) under conditions (photocatalysts loading = 1 $g.L^{-1}$, pH = 3) conventionally employed in most of the previous studies. The results are summarized in Table 3 which show that the PB-modified TiO_2 aerogel reported herein shows excellent photocatalytic performance in both non-acidified (k_{obs} = 0.1074 min^{-1}) and acidified media (k_{obs} = 0.3197 min^{-1}), outperforming most of the already reported TiO_2 materials (k_{obs} < 0.1 min^{-1}) under the experimental conditions employed. Importantly, such high photocatalytic performance is achieved without using any organic reagent as sacrificial electron donor

In order to evaluate the reusability of the material, we carried out repeated Cr(VI) photoreduction tests employing the recycled photocatalysts (Fig. S6). The PB-modified TiO_2 offers limited reusability at the unadjusted pH (pH 5.6), showing large decrease in Cr(VI) removal performance after the second cycle. Such behavior is

probably related to deposition of $Cr(OH)_3$ on the surface of the photocatalyst under unadjusted pH conditions, thereby inactivating the photoactive sites. Nevertheless, under acidic conditions, the photocatalytic material demonstrate excellent reusability and shows no significant decrease in photocatalytic activity after 4 cycles ((Fig. S7).

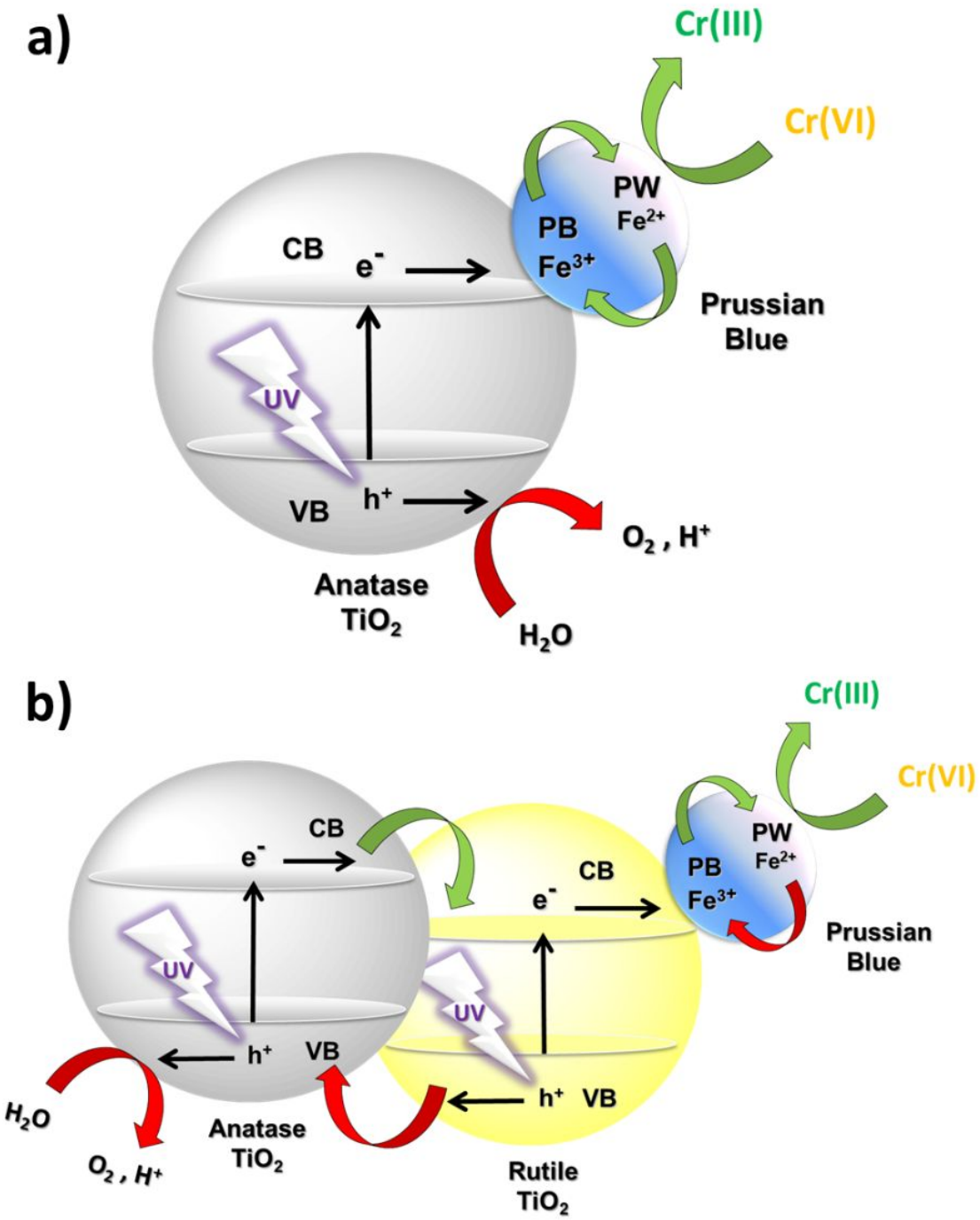

Figure 11. Illustrative scheme of the proposed mechanism for enhanced photocatalytic reduction of (a) phase-pure anatase-PB and (b) mixed anatase-rutile heterojunction-PB. PB stands for “Prussian Blue”, while PW stands for “Prussian White”, the reduced form of PB.

Table 3. Comparison of the Cr(VI) photocatalytic reduction activity in terms of observed kinetic rate constant (k_{obs}) of PB-modified TiO_2 aerogel (TiO_2-EAG-PB2) with other TiO_2 based photocatalysts reported in the literature.

Photocatalyst	**Cr(VI) concentration**	**pH**	**k_{obs} (min^{-1})**	**Catalyst dosage**	**Hole Scavenger**	**Reference**
Prussian Blue-TiO_2 aerogel	10 $mg.L^{-1}$	Unaltered 5-6	0.1074	0.5 $g.L^{-1}$	No	This study
Prussian Blue-TiO_2 aerogel	10 $mg.L^{-1}$	3	0.3197	1.0 $g.L^{-1}$	No	This study
Graphene-Carbon Nanotube-TiO_2	10 $mg.L^{-1}$	Unaltered 6-7	0.00631	0.5 $g.L^{-1}$	No	[53]
ZnO-TiO_2	20 $mg.L^{-1}$	3	0.0879	1 $g.L^{-1}$	No	[54]
TiO_2 (P25)	10 $mg.L^{-1}$	3	0.00171	0.5 $g.L^{-1}$	No	[55]
BiOI-TiO_2	10 $mg.L^{-1}$	Unaltered	0.0465	0.5 $g.L^{-1}$	No	[56]
AgI-TiO_2	8.3 $mg.L^{-1}$	2	0.331	1 $g.L^{-1}$	EDTA	[57]
AgI-TiO_2	8.3 $mg.L^{-1}$	2	0.046	1 $g.L^{-1}$	No	[57]
Ag-TiO_2	10 $mg.L^{-1}$	3	0.052	Thin film	No	[58]
Nd-TiO_2	10 $mg.L^{-1}$	3	0.0486	1 $g.L^{-1}$	Formic Acid	[59]
NiO-TiO_2	20 $mg.L^{-1}$	3.5	0.091	1 $g.L^{-1}$	No	[60]
Poly(fluorene-co-thiophene)-TiO_2	15 $mg.L^{-1}$	3	0.0252	1 $g.L^{-1}$	Phenol	[61]
C_3N_4-F doped TiO_2	20 $mg.L^{-1}$	Unaltered	0.0496	1 $g.L^{-1}$	No	[62]
Ag-P doped TiO_2 fibers	10 $mg.L^{-1}$	3	0.085	1 $g.L^{-1}$	No	[63]

4. Conclusions

In this study, we explored for the first time the role of Prussian blue (PB) as a co-catalyst to improve the photocatalytic properties of TiO_2 and SiO_2-TiO_2 based materials towards photoreduction of Cr(VI). The base photocatalysts particles (TiO_2 and core@shell SiO_2@TiO_2) and aerogels (TiO_2, core@shell SiO_2@TiO_2 and mixed SiO_2-TiO_2) were coated with different amounts (1.7–12.8% Fe) of nanocrystalline PB using a very reproducible photodeposition method. The formation of PB was confirmed by SEM, XRD and vibrational spectroscopy characterization. For a given irradiation time (1h) and precursors ($K_3[Fe(CN)_6]$, $Fe(NO_3)_3$) concentration, the %Fe loading of different TiO_2-materials mentioned above was almost similar (Fe = 3–3.7%), indicating that the amount of photodeposited PB does not vary significantly with the type or chemical composition of titania or silica-titania photocatalysts. The Cr(VI) photoreduction tests demonstrated that all the PB-modified photocatalysts (both aerogels and particles) possess higher photocatalytic activity than the respective unmodified photocatalysts (up to 9 times faster photocatalytic reduction). Remarkably, this occured in deionized water and in the absence of electron donor (hole scavenger) organic molecules. Highest photocatalytic performance was achieved by bycrystalline anatase-rutile TiO_2 aerogel modified with Prussian Blue, thus suggesting that titania phase composition plays an important role on the overall efficiency of PB as a photocatalytic reduction co-catalyst. Moreover, the photocatalytic activity of the samples was dependent on the PB loading and samples with 3–3.7% Fe (PB2 series) exhibited the highest photoactivity (85–99% Cr(VI) photoreduction in 1h) as compared to unmodified photocatalysts (20–40% reduction). Considering the ease with which PB can be incorporated, *via* photodeposition method, into the surface of several classes of photocatalysts, including TiO_2, we believe that the work described herein opens up new possibilities for the preparation of several other photocatalyst/PB systems with improved photocatalytic activities towards Cr (VI) reduction and other target application.

5. Acknowledgements

This work was supported by São Paulo Research Foundation (FAPESP) [research grants no. 2013/24948-3, 2015/22828-6, 2016/10939-0, 2018/01934-0 and 2018/19785-1]. This work was also partially performed under the auspices of the U.S. Department of Energy by Lawrence Livermore National Laboratory under Contract DEAC52-07NA27344. Elias P. Ferreira-Neto thanks FAPESP for PhD and pos-doctoral fellowships [grants # 2013/24948-3 and # 2018/01934-0]. S. Ullah acknowledges financial support from Higher Education Commission, Pakistan [Project No. 9286].The authors acknowledge the Brazilian funding agencies (CNPq and CAPES) for financial assistance. Amanda P. Perissinotto thank the Coordination for the Improvement of Higher Education Personnel (CAPES, Brazil) for PhD fellowship.

6. References

1 L. Rizzo, S. Malato, D. Antakyali, V. G. Beretsou, M. B. Đolić, W. Gernjak, E. Heath, I. Ivancev-Tumbas, P. Karaolia, A. R. Lado Ribeiro, G. Mascolo, C. S. McArdell, H. Schaar, A. M. T. Silva and D. Fatta-Kassinos, *Sci. Total Environ.*, 2019, **655**, 986–1008.

2 P. Borah, M. Kumar and P. Devi, eds. P. Devi, P. Singh and S. K. B. T.-I. P. in W. Kansal, Elsevier, 2020, pp. 17–31.

3 C. F. Carolin, P. S. Kumar, A. Saravanan, G. J. Joshiba and M. Naushad, *J. Environ. Chem. Eng.*, 2017, **5**, 2782–2799.

4 J. J. Coetzee, N. Bansal and E. M. N. Chirwa, *Expo. Heal.*, 2020, **12**, 51–62.

5 M. Nur-E-Alam, M. A. S. Mia, F. Ahmad and M. M. Rahman, *Appl. Water Sci.*, 2020, **10**, 205.

6 C. He, L. Gu, Z. Xu, H. He, G. Fu, F. Han, B. Huang and X. Pan, *Environ. Chem. Lett.*, 2020, **18**, 561–576.

7 S. K. Loeb, P. J. J. Alvarez, J. A. Brame, E. L. Cates, W. Choi, J. Crittenden, D. D. Dionysiou, Q. Li, G. Li-Puma, X. Quan, D. L. Sedlak, T. David Waite, P. Westerhoff and J.-H. Kim, *Environ. Sci. Technol.*, 2019, **53**, 2937–2947.

8 B. Ohtani, *Phys. Chem. Chem. Phys.*, 2014, **16**, 1788–1797.

9 M. I. Litter, *Pure Appl. Chem.*, 2015, **87**, 557–567.

10 Z. Zhao, H. An, J. Lin, M. Feng, V. Murugadoss, T. Ding, H. Liu, Q. Shao, X. Mai, N. Wang, H. Gu, S. Angaiah and Z. Guo, *Chem. Rec.*, 2019, **19**, 873–882.

11 Q. Cheng, C. Wang, K. Doudrick and C. K. Chan, *Appl. Catal. B Environ.*, 2015, **176**–**177**, 740–748.

12 L. Wang, N. Wang, L. Zhu, H. Yu and H. Tang, *J. Hazard. Mater.*, 2008, **152**, 93–99.

13 E. P. Ferreira-Neto, S. Ullah, T. C. A. da Silva, R. R. Domeneguetti, A. P. Perissinotto, F. S. de Vicente, U. P. Rodrigues-Filho and S. J. L. Ribeiro, *ACS Appl. Mater. Interfaces*, 2020, **12**, 41627–41643.

14 K. H. and H. I. and A. Fujishima, *Jpn. J. Appl. Phys.*, 2005, **44**, 8269.

15 K. Nakata and A. Fujishima, *J. Photochem. Photobiol. C Photochem. Rev.*, 2012, **13**, 169–189.

16 K. Suttiponparnit, J. Jiang, M. Sahu, S. Suvachittanont, T. Charinpanitkul and P. Biswas, *Nanoscale Res Lett*, 2010, **6**, 1–8.

17 F. Pellegrino, L. Pellutiè, F. Sordello, C. Minero, E. Ortel, V.-D. Hodoroaba and V. Maurino, *Appl. Catal. B Environ.*, 2017, **216**, 80–87.

18 D. a. H. Hanaor and C. C. Sorrell, *J. Mater. Sci.*, 2011, **46**, 855–874.

19 B. Ohtani, *Catalysts*, 2013, **3**, 942–953.

20 M. Pelaez, N. T. Nolan, S. C. Pillai, M. K. Seery, P. Falaras, A. G. Kontos, P. S. M. Dunlop, J. W. J. Hamilton, J. A. Byrne, K. O'Shea, M. H. Entezari and D. D. Dionysiou, *Appl. Catal. B Environ.*, 2012, **125**, 331–349.

21 H. Wang, L. Zhang, Z. Chen, J. Hu, S. Li, Z. Wang, J. Liu and X. Wang, *Chem. Soc. Rev.*, 2014, **43**, 5234–5244.

22 M. Dahl, Y. Liu and Y. Yin, *Chem. Rev.*, 2014, **114**, 9853–9889.

23 A. Ludi, *J. Chem. Educ.*, 1981, **58**, 1013.

24 M. Ware, *J. Chem. Educ.*, 2008, **85**, 612.

25 K. Dunbar and R. Heintz, *Prog. Inorg. Chem.*, 1997, **45**, 283–391.

26 L.-M. Cao, D. Lu, D.-C. Zhong and T.-B. Lu, *Coord. Chem. Rev.*, 2020, **407**, 213156.

27 J. Chen, L. Wei, A. Mahmood, Z. Pei, Z. Zhou, X. Chen and Y. Chen, *Energy Storage Mater.*, 2020, **25**, 585–612.

28 K. Szaci?owski, W. Macyk and G. Stochel, *J. Mater. Chem.*, 2006, **16**, 4603–4611.

29 B. Seelandt and M. Wark, *Microporous Mesoporous Mater.*, 2012, **164**, 67–70.

30 H. Tada, Y. Saito and H. Kawahara, *J. Electrochem. Soc.*, 1991, **138**, 140–144.

31 T. Yamamoto, N. Saso, Y. Umemura and Y. Einaga, *J. Am. Chem. Soc.*, 2009, **131**, 13196–7.

32 L. Han, L. Bai and S. Dong, *Chem. Commun.*, 2014, **50**, 802–804.

33 X. Li, J. Wang, A. I. Rykov, V. K. Sharma, H. Wei, C. Jin, X. Liu, M. Li, S. Yu, C. Sun and D. D. Dionysiou, *Catal. Sci. Technol.*, 2015, **5**, 504–514.

34 S. Husmann, L. F. Lima, L. S. Roman and A. J. G. Zarbin, *ChemSusChem*, 2018, **11**, 1238–1245.

35 H. Kim, M. Kim, W. Kim, W. Lee and S. Kim, *J. Hazard. Mater.*, 2018, **357**, 449–456.

36 R. Chen, Q. Zhang, Y. Gu, L. Tang, C. Li and Z. Zhang, *Anal. Chim. Acta*, 2015, **853**, 579–587.

37 S. Xing, H. Xu, G. Shi, J. Chen, L. Zeng and L. Jin, *Electroanalysis*, 2009, **21**, 1678–1684.

38 E. P. Ferreira-Neto, S. Ullah, M. B. Simões, A. P. Perissinotto, F. S. de Vicente, P.-L. M. Noeske, S. J. L. Ribeiro and U. P. Rodrigues-Filho, *Colloids Surfaces A Physicochem. Eng. Asp.*, 2019, **570**, 293–305.

39 E. P. Ferreira-Neto, M. A. Worsley and U. P. Rodrigues-Filho, *J. Environ. Chem. Eng.*, 2019, **7**, 103425.

40 E. P. Ferreira Neto, S. Ullah, V. P. Martinez, J. M. S. C. Yabarrena, M. B. Simões, A. P. Perissinotto, H. Wender, F. S. de Vicente, M. Noeske, S. J. L. Ribeiro and U. P. Rodrigues-Filho, *Mater. Adv.*, , DOI:10.1039/D0MA00785D.

41 G. Leofanti, M. Padovan, G. Tozzola and B. Venturelli, *Catal. Today*, 1998, **41**, 207–219.

42 T. Matthias, K. Katsumi, N. A. V, O. J. P, R.-R. Francisco, R. Jean and S. K. S. W, *Pure Appl. Chem.*, 2015, 87, 1051.

43 K. Ueno, T. Imamura and K. L. Cheng, *Handbook of Organic Analytical Reagents*, CRC Press, 2ª., 1992.

44 S. F. A. Kettle, E. Diana, E. M. C. Marchese, E. Boccaleri and P. L. Stanghellini, *J. Raman Spectrosc.*, 2011, **42**, 2006–2014.

45 A. N. Murashkevich, A. S. Lavitskaya, T. I. Barannikova and I. M. Zharskii, *J. Appl. Spectrosc.*, 2008, **75**, 730–734.

46 P. J. Kulesza, M. A. Malik, A. Denca and J. Strojek, *Anal. Chem.*, 1996, **68**, 2442–2446.

47 L. Samain, F. Grandjean, G. J. Long, P. Martinetto, P. Bordet and D. Strivay, *J. Phys. Chem. C*, 2013,

117, 9693–9712.

48 S. Umapathy, A. J. McQuillan and R. E. Hester, *Chem. Phys. Lett.*, 1990, **170**, 128–132.

49 M. Valari, A. Antoniadis, D. Mantzavinos and I. Poulios, *Catal. Today*, 2015, **252**, 190–194.

50 S. Luo, Y. Xiao, L. Yang, C. Liu, F. Su, Y. Li, Q. Cai and G. Zeng, *Sep. Purif. Technol.*, 2011, **79**, 85–91.

51 M. I. Litter, *Pure Appl. Chem.*, 2015, 87, 557.

52 S. Nappini, A. Matruglio, D. Naumenko, S. Dal Zilio, M. Lazzarino, F. M. F. De Groot, C. Kocabas, O. Balci and E. Magnano, *J. Phys. Chem. C*, 2017, **121**, 22225–22233.

53 C. Wang, M. Cao, P. Wang, Y. Ao, J. Hou and J. Qian, *Appl. Catal. A Gen.*, 2014, **473**, 83–89.

54 M. Naimi-Joubani, M. Shirzad-Siboni, J. K. Yang, M. Gholami and M. Farzadkia, *J. Ind. Eng. Chem.*, 2015, **22**, 317–323.

55 Y. Ku and I. L. Jung, *Water Res.*, 2001, **35**, 135–142.

56 J. Xu, J. Zhu and M. Chen, *J. Mol. Liq.*, 2020, **320**, 114479.

57 Q. Wang, X. Shi, J. Xu, J. C. Crittenden, E. Liu, Y. Zhang and Y. Cong, *J. Hazard. Mater.*, 2016, **307**, 213–220.

58 S. Wang, Z. Zhang, W. Huo, K. Zhu, X. Zhang, X. Zhou, F. Fang, Z. Xie and J. Jiang, *J. Hazard. Mater.*, 2020, **399**, 123016.

59 S. Rengaraj, S. Venkataraj, J. W. Yeon, Y. Kim, X. Z. Li and G. K. H. Pang, *Appl. Catal. B Environ.*, 2007, **77**, 157–165.

60 Y. Ku, C. N. Lin and W. M. Hou, *J. Mol. Catal. A Chem.*, 2011, **349**, 20–27.

61 R. Qiu, D. Zhang, Z. Diao, X. Huang, C. He, J. L. Morel and Y. Xiong, *Water Res.*, 2012, **46**, 2299–2306.

62 J. Wang, W. Lin, H. Hu, C. Liu, Q. Cai, S. Zhou and Y. Kong, *New J. Chem.*, 2021, **45**, 3067–3078.

63 S. Ghafoor, F. Aftab, A. Rauf, H. Duran, K. Kirchhoff and S. N. Arshad, *ChemistrySelect*, 2020, **5**, 14078–14085.